



# Influence of Microalloying and Isothermal Treatment on Microstructure and Mechanical Properties of High Carbon Steel

Indrajit Dey<sup>1</sup> · Rajib Saha<sup>2</sup> · Swarup Kumar Ghosh<sup>1</sup>

Received: 23 March 2021 / Accepted: 31 May 2021 / Published online: 27 September 2021  
© The Korean Institute of Metals and Materials 2021

## Abstract

The influence of isothermal holding (IH) near the pearlite start temperature ( $P_s \approx 610$  °C) and above the martensite start temperature ( $M_s \approx 245$  °C) were studied in two hot-rolled (FRT  $\approx 1000$  °C) high carbon steels, without (HC0) and with Nb microalloying (HC1). Optical microscopy (OM), field emission scanning electron microscopy (FESEM) and high-resolution transmission electron microscopy (HRTEM) were utilised for observing the microstructural constituents whereas, nanoindentation and microindentation were performed to estimate the average hardness and elastic modulus values of various phase constituents. It has been observed that hot deformation in the austenite region results in the formation of a dual phase-type microstructure consisting of fine pearlite lamella and ferrite grains with some amount of degenerated pearlite. IH at 570 °C leads to a higher volume percentage of ferrite and coarsening of pearlite whereas, IH at 300 °C results in mixed phases comprising bainite, a very low amount of martensite/retained austenite (M/RA), pearlite and some amount of ferrite. Hot rolled microalloyed steel when isothermally held near the  $P_s$  results in a significant enhancement of ductility than hot rolled and air-cooled condition while sacrificing tensile strength marginally, which may be attributed to a higher percentage of ferrite and refinement of pearlite due to Nb addition. The estimated yield strength values correlate well with those experimental yield strength values, but a little discrepancy has been noticed for the ultimate tensile strength values. Possible interpretations are suggested in this paper.

**Keywords** High carbon steel · Microalloying · Microstructure · Nanoindentation · Yield strength

## 1 Introduction

Thermomechanical treatments with controlled finish rolling temperature (FRT) followed by isothermal holding (IH) for a certain duration or direct quenching after successful completion of the rolling have been considered as an effective energy-saving technology [1, 2]. The benefit is, the steel products made from the toughening steels through the thermomechanical methods, require tempering only whereas, the conventional heat treatment process includes both quenching and tempering [3]. Hot deformation with controlled FRT is effective for tailoring the mechanical properties of

hot-rolled steel products [1–9]. The hot deformation behaviour of microalloyed steels can be affected by various factors, among which chemical composition is a major one. Some researchers have agreed that with the increasing carbon content, the work hardening rate can be lowered with the deformation temperatures of 850–1300 °C. On the contrary, some have opined that the hot flow behaviour of austenite at 900–1100 °C is not affected by the carbon content [3–9].

Austenite grain size (AGS) before quenching plays a major role in influencing the phase transformations, precipitation and thereby mechanical properties [10–12]. The addition of various alloying elements in carbon steels, is beneficial to reduce the grain growth rate either by the solute dragging effect or by effective pinning by the carbides or nitride precipitates in austenite [10–12]. Niobium (Nb) microalloying is beneficial for structural steels due to considerable enhancement in mechanical properties. Several studies on Nb (C, N) precipitation kinetics in the austenite matrix have been carried out to date because these precipitates trigger strong retardation on the recrystallization of

✉ Swarup Kumar Ghosh  
skghosh@metal.iests.ac.in

<sup>1</sup> Department of Metallurgy & Materials Engineering,  
Indian Institute of Engineering Science and Technology,  
Shibpur, Howrah 711103, India

<sup>2</sup> Product Development Research Group, R & D Division, Tata  
Steel Limited, Jamshedpur 831007, India

austenite. Many researchers have opined that plastic deformation enhances the precipitation kinetics in austenite due to the incidence of deformation-induced high dislocation density [13–15].

High carbon steel wire rods with near eutectoid compositions have been widely used for manufacturing bolts, springs, metal cords, steel cables as well as to produce prestressed concrete wires of huge structures like suspension bridges, buildings, large concrete pipes etc. [16–22]. These wire rods can be produced as per industrial practices where hot rolling of the billets are generally adapted with FRT of 800–1050 °C followed by either continuous cooling with air-blasting or isothermal holding (IH) in a salt bath furnace. Earlier investigation [21] suggests that better mechanical properties with ultimate tensile strength (UTS $\approx$ 1207 MPa) and total elongation (TEL $\approx$ 13.2%) can be achieved with ferrite-pearlite microstructure in case of a 0.82C-0.21Si-0.68Mn-0.01P-0.009S-0.003 N (wt%) steel during isothermal transformation at 560 °C, which is suitable for wire drawing application. An excellent combination of mechanical properties with cold drawability has been also reported earlier by lead patenting at 540–560 °C [21, 23]. So, in the present research, an attempt has been taken to find out the influence of IH near pearlite start temperature ( $P_s$ ) to stimulate the actual industrial conditions [21].

The possibility of achieving mixed-phase microstructures with various heat treatment schedules has pushed the researchers to further investigate the effect of various microstructural constituents on the mechanical properties of various high strength, multiphase low alloy steels. A study has been recently carried out with a 0.411C-0.225Si-0.624Mn-0.018S-0.017P (wt%) steel to achieve ultimate tensile strength (UTS $\approx$ 770 MPa), yield strength (YS $\approx$ 491 MPa) with total elongation (TEL $\approx$ 12.5%) for ferrite-pearlite-martensite multiphase microstructures [24]. Therefore, it will be interesting to conduct IH near martensite start temperature ( $M_s$ ) to get multiphase microstructures comprising ferrite-bainite-martensite with some amount of pearlite as an additional microstructural constituent and to reach the favourable mechanical properties.

For the past few years, nanoscratch and nanoindentation techniques have been considered an effective tool for investigating various steels by giving important information about the mechanical properties in both elastic and plastic regions with higher spatial resolution [25–27]. It is well known that nanoindentation is a depth-sensing indentation technique where the indentation size effect (ISE) and surface

roughness play a major role while determining the hardness values [28, 29]. It has been reported earlier that, in the case of a complex structure like pearlite, the fine-lamella with nonequilibrium structure exhibits higher values of elastic modulus than the coarse-lamellar pearlite [30]. In this paper, indentation depth profiles of the nanohardness and its variations with the microstructural constituents have been extensively investigated for high carbon hot rolled steel plates as well as for isothermally treated samples.

Besides nanoindentation, microindentation at low loads has been already reported as an effective technique for confirming the existence of different phases in the microstructure as well as for evaluating numerous mechanical properties (e.g., fracture stress, Young's modulus, flow stress, fracture toughness etc.) [31, 32]. However, inadequate studies have been carried out to date on this aspect for high carbon steel particularly with Nb microalloying. Therefore, it is expected that all the experimental proofs given in this paper will expand the scope of knowledge on various microstructural constituents that govern the hardness and strength of high carbon steel.

## 2 Experimental Procedure

### 2.1 Processing of the Experimental Steels

In the present research, two high carbon steels with Nb microalloying (HC1) and without microalloying (HC0) were obtained from Tata Steel, Jamshedpur, India in the form of forged bars. The chemical compositions of these two investigated steels are listed in Table 1.

The forged specimens (initial thickness of  $\sim$ 25 mm) were heated at 1200 °C for 1 h for complete homogenisation. All these homogenised samples were immediately subjected to hot rolling operation in the austenite region with a finish rolling temperature (FRT) of 1000 °C and then air-cooled to room temperature. An optical pyrometer was used to maintain the required temperature constantly after each rolling pass and the rolling has been scheduled in such a way that the temperature after the first four passes has been maintained at 1150 °C, for the next four passes the temperature has been kept  $\approx$ 1100 °C and thus continuing up to the FRT $\approx$ 1000 °C. After successful completion of the hot rolling, the hot-rolled plates (with a final thickness of  $\approx$ 6 mm) were further austenitised at 900 °C for 45 min and then subjected to IH at 570 °C (near  $P_s$  $\approx$ 610 °C) and 300 °C

**Table 1** The chemical compositions of the two investigated alloys (wt%)

Alloy Code	C	Mn	Si	Nb	S	P	Fe
HC0	0.66	0.67	0.20	–	0.006	0.014	Bal.
HC1	0.66	0.67	0.20	0.03	0.006	0.014	Bal.

(above  $M_s \approx 254$  °C) each for 30 min duration in a salt bath furnace followed by air cooling to room temperature. It is important to mention that both the  $P_s$  and  $M_s$  temperatures were obtained from the dilatometric experiments by using a Gleeble 3800 simulator. It has been observed that these values fit well with those estimated values which were being calculated from the standard empirical formulas with a maximum variation of  $\pm 10$  °C. Therefore, the isothermal holding temperatures near  $P_s$  and above  $M_s$  were chosen in such a way that, there may be a maximum variation of  $\approx +50$  °C. The schematic diagram of the rolling and heat treatment schedule has been presented in Fig. 1.

## 2.2 Micro-Structure Analysis

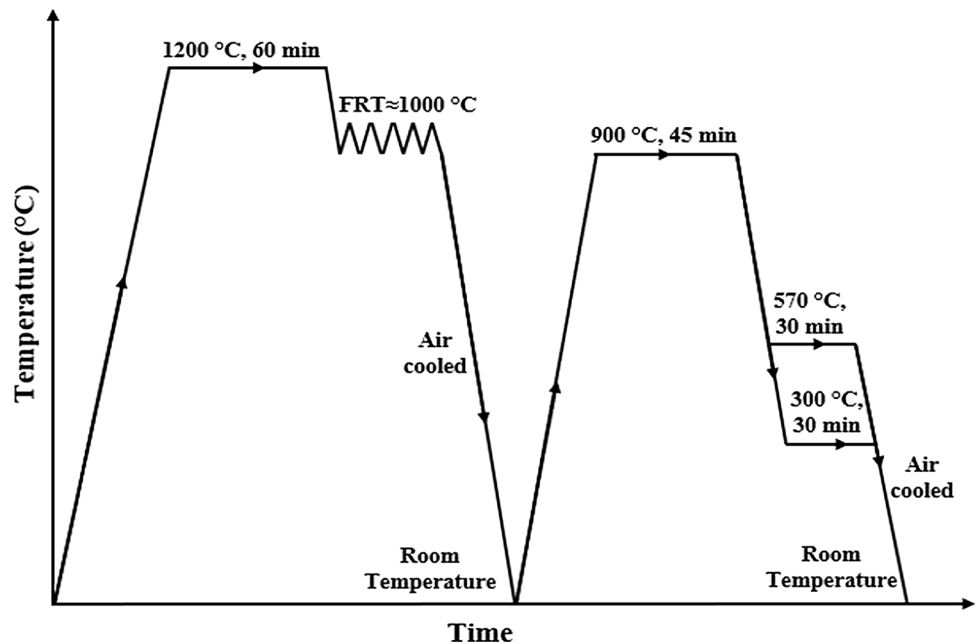
The as-rolled samples were prepared suitably by maintaining some standard metallographic specimen preparation techniques, such as coarse polishing with emery papers of different grits followed by fine polishing using a selvylt cloth and diamond paste of 1-micron size. Subsequently, etching with 2% nital solution was done to observe the microstructures. An Axiovert 40 Mat (Carl Zeiss) optical microscope, a field emission scanning electron microscope JSM-7610F-FESEM (JEOL) with operating voltage 15–20 kV and a high-resolution transmission electron microscope HRTEM (Tecnai G<sup>2</sup>) with operating voltage 200 kV were utilised to observe the microstructure. Initially, the circular disc of 3 mm diameter was cut from the centre of the mechanically thinned sample ( $\approx 80$   $\mu\text{m}$  thickness). Then electropolishing at 12 °C was adapted using an electrolytic solution of 90% acetic acid and 10% perchloric acid to further reduce the thickness of the samples for observing the microstructural

constituents under HRTEM. The volume percentage of ferrite/pearlite was measured from 15 to 25 consecutive optical micrographs by using an Axiovision image analysis software of version 4.8. The various important parameters like pearlite colony and nodule size were calculated by using the linear intercept method from approximately 20–30 numbers of high-resolution FESEM micrographs whereas, 12–18 numbers of HRTEM micrographs were utilised to measure the average values of interlamellar spacing and cementite thickness using a HRTEM analysis software namely, Gatan Microscopy Suite 1.8.3 under Gatan Digital Micrograph [33, 34].

## 2.3 Hardness Evaluation

To perform the Vickers hardness test, the Innovatest Ver-zus 750 CCD Universal hardness tester was utilised to get the bulk hardness under a load of 30 kg and dwell time of 20 s. Fifteen to twenty indentations on each sample were taken for calculating the average hardness value. Vickers Microhardness Tester (Leica VMHT) was utilised for measuring the microhardness values and the load and dwelling time were kept at 10 gf and 20 s, respectively. These Vickers microindentations were further visualised under the scanning electron microscope (SEM) (Hitachi) to identify the phase constituents in the microstructure. Nanoindentation was performed with the help of Hysitron TI 950 TriboIndenter under the load of 5000  $\mu\text{N}$  and the loading, holding and unloading time were kept 10 s-10 s-10 s, respectively. A diamond Berkovich indenter, with an indenter radius of 100 nm was equipped with this apparatus. Approximately 30 to 40 nanoindentations were

**Fig. 1** A typical representation of hot rolling and heat treatment schedule





taken at several spots on the mirror-like polished samples and hardness and elastic modulus were determined as a function of indentation depth.

## 2.4 Tensile Testing

For tensile testing, flat specimens (~3.1 mm thick) having a gauge length of 25 mm were prepared from the longitudinal direction of hot rolled plates following the ASTM E8M standard and for this purpose, an Instron 5900R testing machine coupled with an extensometer was utilised with the crosshead velocity of 0.5 mm/min. After completion of tensile testing, the morphology of the tensile fracture surface was observed by using FESEM.

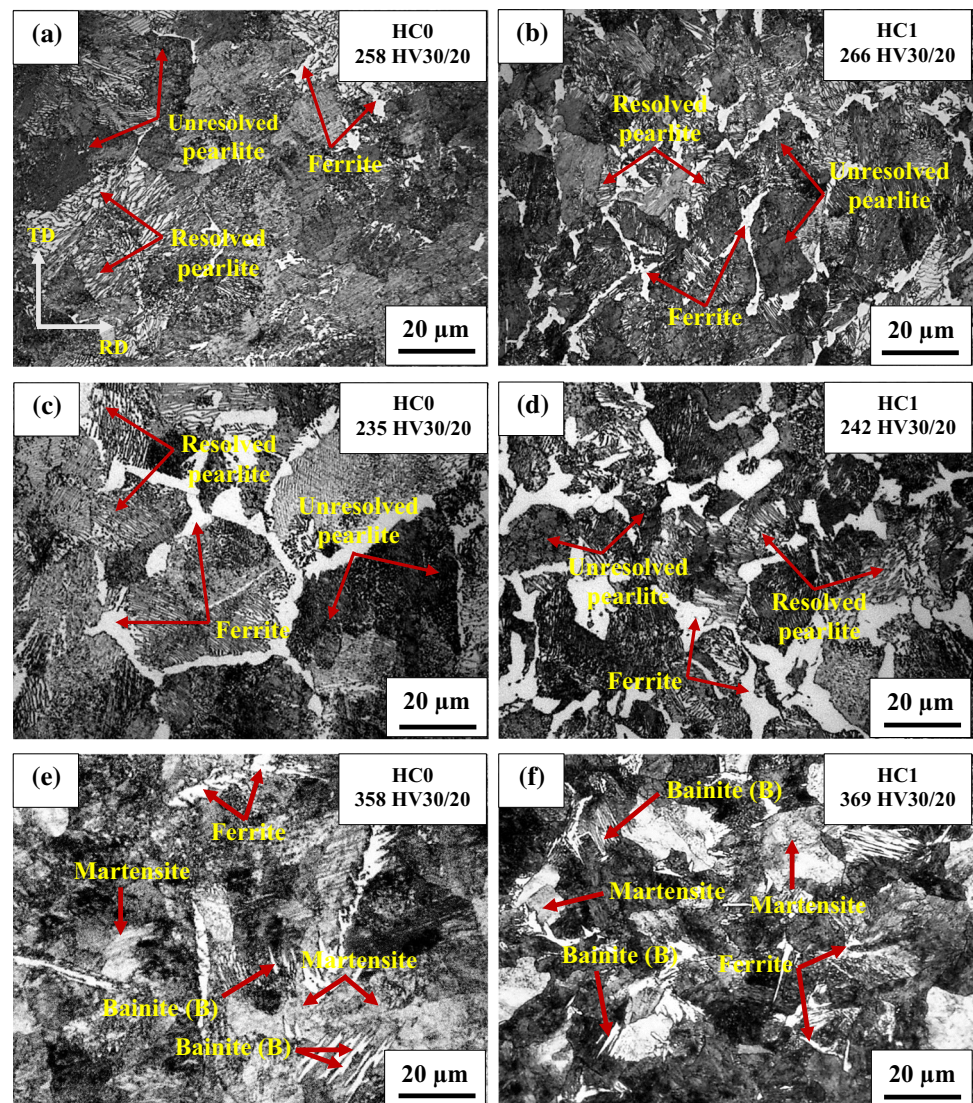
## 3 Results and Discussion

### 3.1 Microstructure Characterisation

#### 3.1.1 Formation of Different Phases

Figure 2a and b represent the optical micrographs of hot rolled air-cooled samples of HC0 and HC1 steels, respectively. Figure 2c to f represent the optical micrographs of hot rolled air-cooled samples subjected to isothermal holding (IH) near the  $P_s$  (570 °C) and at above  $M_s$  (300 °C) temperatures for both HC0 and HC1 steels, respectively. The rolling direction (RD) and transverse direction (TD) have been shown in Fig. 2a for considering the effect of deformation on microstructure. The rolling axis is perpendicular to the observation plane in all the micrographs. It is noteworthy to mention that for

**Fig. 2** Optical micrographs of hot rolled and air-cooled samples **a** HC0-HRAC-FRT 1000 °C, **b** HC1-HRAC-FRT 1000 °C, isothermally treated samples **c** HC0-FRT 1000 °C-IH 570 °C, **d** HC1-FRT 1000 °C-IH 570 °C and low-temperature isothermally treated samples **e** HC0-FRT 1000 °C-IH 300 °C and **f** HC1-FRT 1000 °C-IH 300 °C. RD: Rolling direction and TD: Transverse direction



hot-rolled samples (Fig. 2a and b) the rolling direction has been revealed whereas, in the case of heat-treated samples (Fig. 2c to 2f), it seems to be unclear which may be correlated with the fact that the residual or arrested strain after hot rolling was present, while after isothermal holding heat treatment it has been relieved. Although no clear evidence of recrystallization was observed, the microstructures can be characterised by equiaxed grains after heat treatment, which agrees well with the previous reports [35, 36].

Figure 2a to d mainly reveal a two-phase microstructure consisting of ferrite and pearlite (resolved/unresolved). In resolved pearlite, the alternating lamella of ferrite and cementite can be easily separated due to wide interlamellar spacings, whereas it is not possible in the case of unresolved pearlite due to fine interlamellar spacing. Figures 2e and f show a mixed-phase microstructure consisting of bainite lath, ferrite, unresolved pearlite and martensite phases as denoted by arrows in those micrographs. It may be mentioned that the possibility of the formation of some amount of retained austenite can't be overruled as the steels have been subjected to IH above  $M_s$  (300 °C) temperature [37–42]; however, it is very difficult to identify its presence in these optical micrographs. It is obvious that in Fig. 2a to f, milky white contrast reveals the ferrite phase whereas, greyish contrast represents martensite. Bainite which is a combination of cementite and dislocation rich ferrite is usually revealed as a lenticular plate or lath morphology in the dark region as shown in Fig. 2e and f. It has been observed that all the optical micrographs contain pearlite in the final microstructure after the low-temperature isothermal holding treatment, whose incidence may be related to free cooling before quenching from the austenitising temperature.

Average Vickers hardness values are indicated in all the micrographs. It can be noted that the hardness value for HC1 steel is higher compared to HC0 steel. It is well established that the addition of Nb, as a microalloying element is responsible for decreasing temperatures for phase transformation and contributes to the refinement of pearlite colony size and pearlite interlamellar spacing [40, 43] and thereby, results in higher hardness.

Table 2 summarises the values of the volume percentage of different phases present in the microstructures of hot rolled air-cooled samples as well as isothermally treated samples at 570 °C for both the steels. It has been observed that the ferrite percentage in HC1 steel is more than HC0 steel, which is due to the fact that Nb is a ferrite stabiliser [44]. The percentage of ferrite has been increased in the case of hot rolled air-cooled samples when isothermally held at 570 °C for both the steels which may be related to free cooling before isothermal holding at 570 °C.

**Table 2** Volume percentage of microstructural constituents of hot rolled air-cooled and heat-treated (isothermal holding at 570 °C) samples

Sample condition	Volume percentage (%)	
	Ferrite	Pearlite
HC0-HRAC-FRT 1000 °C	7 ± 1	93 ± 5
HC1-HRAC-FRT 1000 °C	15 ± 2	85 ± 5
HC0-HRAC-FRT 1000 °C-IH 570 °C	18 ± 2	82 ± 5
HC1-HRAC-FRT 1000 °C-IH 570 °C	28 ± 2	72 ± 4

### 3.1.2 Estimation of the Different Microstructural Parameters

Figure 3a and b represent the FESEM micrographs of HC0 and HC1 steels after hot rolling followed by air-cooling. Figure 3c to f represent the FESEM micrographs of hot rolled air-cooled samples followed by IH near  $P_s$  (570 °C) and above  $M_s$  (300 °C) temperatures for both HC0 and HC1 steels, respectively. The presence of bainite can be observed in Fig. 3e and f.

Figure 3a to d mainly reveal a two-phase microstructure of ferrite and pearlite for both the HC0 and HC1 steels after hot rolling followed by air-cooling and IH near  $P_s$  (570 °C). Mixed microstructures containing ferrite, bainite, martensite and pearlite can be observed in Fig. 3e and f after IH above  $M_s$  (300 °C) temperatures of both the investigated steels [39–42]. Two high-resolution FESEM micrographs as shown at the insets of Fig. 3e and f reveal bainite as well as some amount of pearlite after IH heat treatment at 300 °C for both the high carbon steels. These micrographs mainly reveal a mixed-phase microstructure containing bainite (B), martensite or retained austenite (M/RA) and carbide, after IH above  $M_s$  [37–49]. The addition of Nb promotes grain refinement which further triggers the transformation kinetics indirectly leading to the formation of pro-eutectoid ferrite and upper bainite [50]. IH at 300 °C leads to the formation of bainite, containing carbide which entraps the carbon strongly and thus remains stable at room temperature avoiding the further conversion of retained austenite. Bainite is present as long, thin sheaves containing carbides in the FESEM micrographs (Fig. 3e and f). It is well known that Nb, being a ferrite stabiliser, along with carbides in bainite, slow down the formation of austenite at room temperature. Interestingly, retained austenite was not detected after isothermal holding, which may be due to the insufficient contents of Mn and Si to stabilise some amount of retained austenite in the investigated steel. In this connection, it is pertinent to mention here that IH at 300 °C results in an increase in hardness than that of isothermal holding at 570 °C which is attributed to the harder phase like bainite formed at 300 °C [45–50].



**Fig. 3** FESEM micrographs of hot rolled and air-cooled samples **a** HC0-HRAC-FRT 1000 °C, **b** HC1-HRAC-FRT 1000 °C, isothermally treated samples **c** HC0-FRT 1000 °C-IH 570 °C, **d** HC1-FRT 1000 °C-IH 570 °C and low-temperature isothermally treated samples **e** HC0-FRT 1000 °C-IH 300 °C and **f** HC1-FRT 1000 °C-IH 300 °C. RD: Rolling direction and TD: Transverse direction

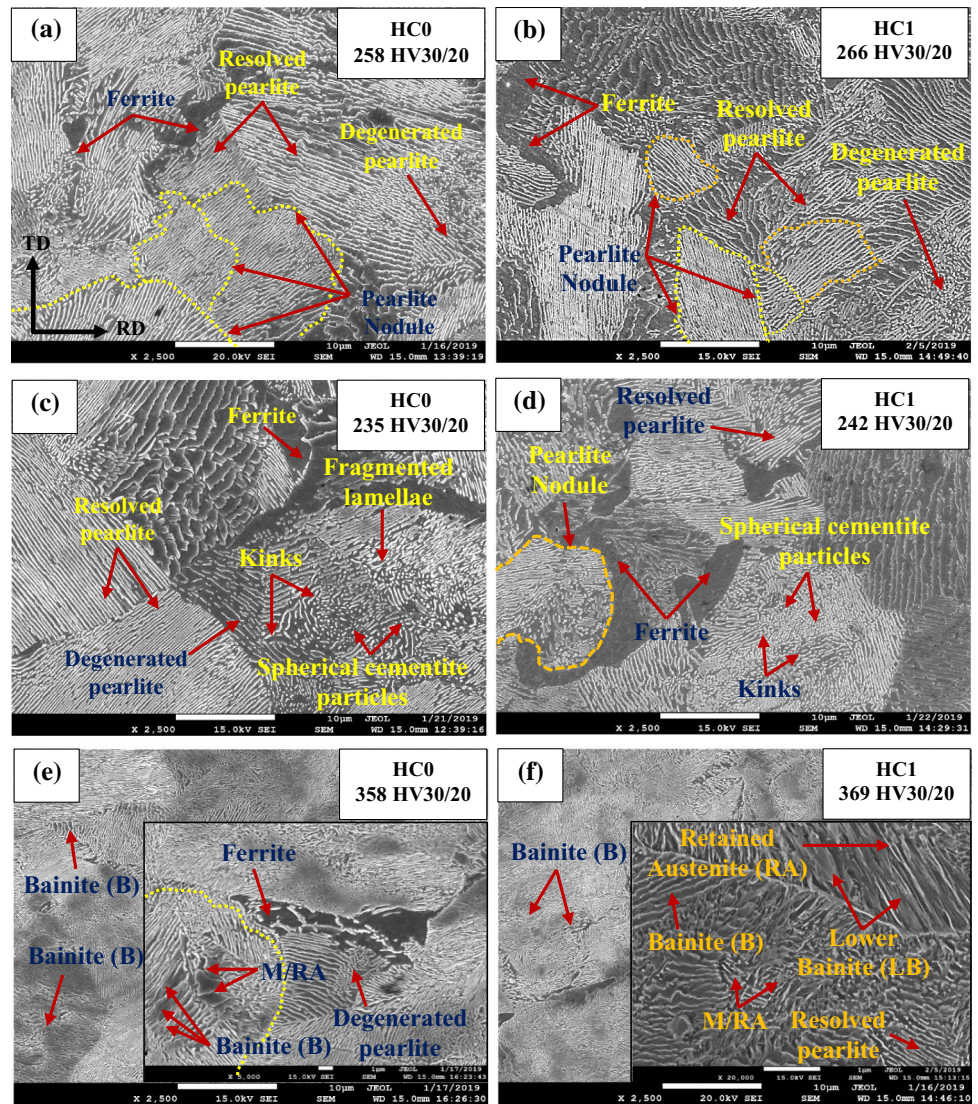


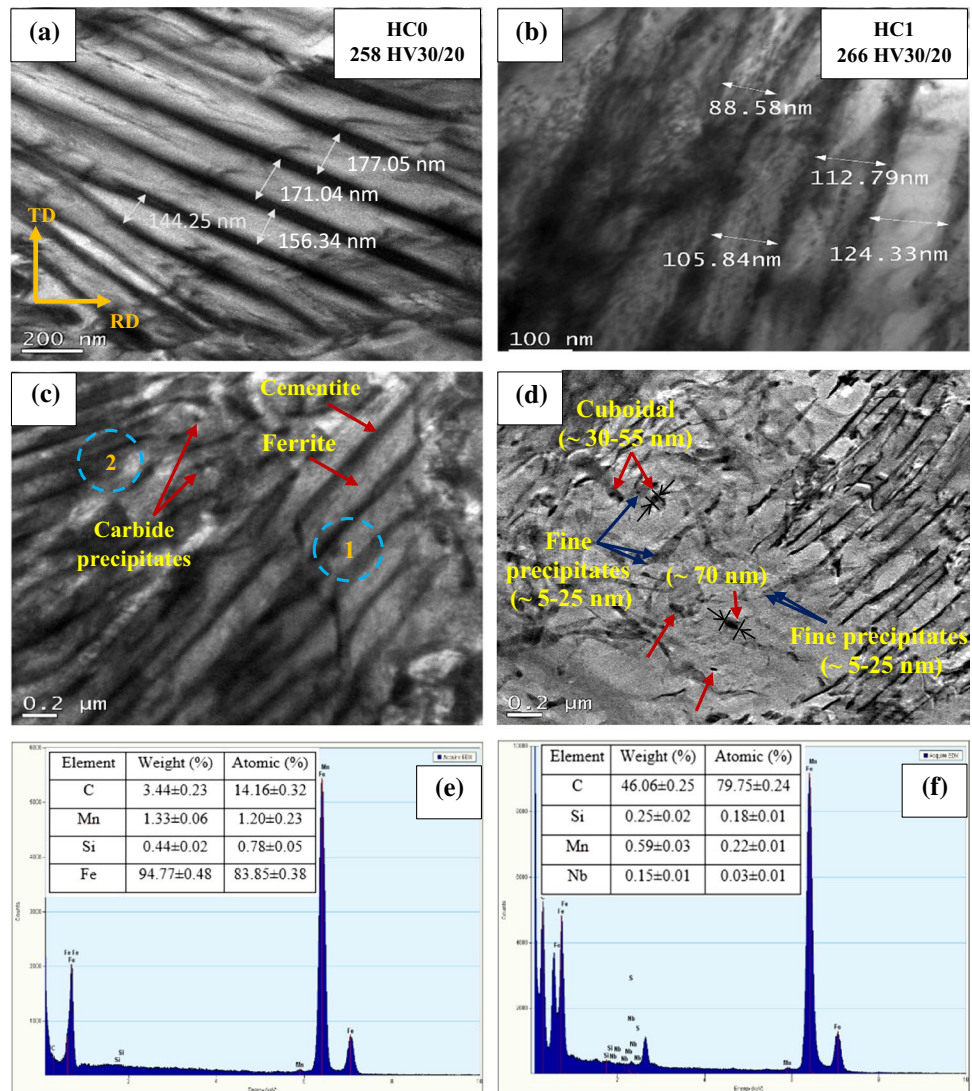
Table 3 summarises the values of prior austenite grain size (PAGS), pearlite nodule size (NS), pearlite colony size (PS), pearlite interlamellar spacing ( $\lambda$ ) as well as cementite thickness (CT) of hot-rolled air-cooled samples with FRT $\approx$ 1000 °C and hot-rolled air-cooled followed by isothermally heat-treated samples at 570°C. It has been observed that PAGS, NS and PS have become finer for hot rolled and air-cooled samples than those of isothermally treated

samples for both the steels. This fact is due to the presence of a greater number of nucleation sites due to a higher cooling rate after hot rolling followed by air cooling and as a result, impingement between nodules occurs and pearlite nodules, as well as colonies, becomes finer. It can be seen from Table 3 and Fig. 4 that pearlite interlamellar spacing is finer in the case of HC1 steel since Nb contributes to the refinement of interlamellar spacing [43]. The interlamellar

**Table 3** Values of prior austenite grain size (PAGS), pearlite nodule size (NS), pearlite colony size (PS), interlamellar spacing ( $\lambda$ ) and cementite thickness (CT) of hot-rolled air-cooled and heat-treated (isothermal holding at 570°C) samples

Sample condition	PAGS ( $\mu\text{m}$ )	NS ( $\mu\text{m}$ )	PS ( $\mu\text{m}$ )	$\lambda$ (nm)	CT (nm)
HC0-HRAC-FRT 1000 °C	58 $\pm$ 4	50 $\pm$ 3	8 $\pm$ 4	150 $\pm$ 15	46 $\pm$ 12
HC1-HRAC-FRT 1000 °C	46 $\pm$ 4	27 $\pm$ 3	5 $\pm$ 3	108 $\pm$ 10	36 $\pm$ 11
HC0-FRT 1000 °C-IH 570 °C	69 $\pm$ 5	59 $\pm$ 4	11 $\pm$ 4	174 $\pm$ 12	96 $\pm$ 10
HC1-FRT 1000 °C-IH 570 °C	50 $\pm$ 5	33 $\pm$ 4	7 $\pm$ 5	154 $\pm$ 24	64 $\pm$ 14

**Fig. 4** Bright field HRTEM micrographs of hot rolled and air-cooled samples, **a** & **c** HC0-HRAC-FRT 1000 °C and **b** & **d** HC1-HRAC-FRT 1000 °C. The dark precipitate of carbide particles (denoted by arrow) in HC0-HRAC-FRT 1000 °C sample and dark precipitate of NbC particles (denoted by arrow) in HC1-HRAC-FRT 1000 °C sample are shown in Figures **c** & **d**, respectively. Corresponding EDS spectrum and chemical compositions of iron carbide and NbC precipitates are shown in Figures **e** & **f**, respectively. RD: Rolling direction and TD: Transverse direction



spacing is finer for hot rolled and air-cooled samples for both the steels than those of isothermally treated samples which are attributed to the fact that hot rolling followed by air-cooling imposed to higher cooling rate whereas, hot rolling followed by IH near  $P_s$  results in interrupted cooling.

### 3.1.3 Formation of NbC Precipitate

Figure 4 reveals the bright field HRTEM micrographs and corresponding EDS analysis of carbide and NbC precipitates in HC0 and HC1 steels, respectively. The measured values of pearlite interlamellar spacing for both the steels are shown in Figs. 4a and b. The addition of Nb leads to refinement in  $\lambda$  values ( $\sim 42$  nm) which is evident in Fig. 4a and b. Figure 4c shows lamellar alternate ferrite-cementite bands in the denoted region (1) as well as degenerated morphology of pearlite in the denoted region (2) and the corresponding EDS spectrum of cementite to distinguish cementite from

ferrite as indicated in Fig. 4e. As the cooling rate increases, the cementite morphology has been reported to change from lamellar to degenerated pearlite and then finally to small cementite particles. The formation of degenerated pearlite can be associated with inadequate carbon diffusion for developing continuous lamellae during cooling and its presence can significantly increase the toughness of the steel [51, 52]. The occurrence of two types of NbC precipitates can be seen in Fig. 4d and the corresponding EDS analysis in Fig. 4f confirms the presence of NbC precipitates in HC1 steel after hot rolling followed by the air-cooling. These two precipitates can be classified depending on their sizes [53]. Firstly, fine NbC precipitates (denoted by arrows) having the size of about  $\sim 5$ – $25$  nm which are present in ferrite matrix as evident in Fig. 4d, significantly contribute to the precipitation strengthening [54]. It has been reported earlier that during isothermal holding these fine precipitates may begin to coarsen due to continuous nucleation and growth



[55]. Secondly, coarse NbC precipitates with an average size ~30–80 nm can be cuboidal, spherical or irregular type as denoted by arrows in Fig. 4d [55, 56]. It impedes the growth of the recrystallised austenite grains. Moreover, deformation in the austenite results in high dislocation density which is desirable for sub-grain boundary formation of the deformed austenite [54]. The presence of cube-like NbC precipitates in Fig. 4d cannot be overruled which nucleates during hot rolling at the austenitisation stage before air-cooling [53]. It has been reported earlier that these cubic B1 (NaCl) type carbides show a cube-cube orientation relationship with the austenite phase [53]. For the present carbon composition, the solubility product of Nb in austenite was calculated by using Eq. (1) [57] as given below.

$$\text{Log} [(Nb\%) \times (C\%)] = \left[ 3.89 - \frac{8030}{T} \right] + \left[ \frac{1150}{T} - 0.05 \right] \times C\% \quad (1)$$

where T is in Kelvin (K).

It has been found that solubility of Nb in HC1 steel rises with increasing temperature, e.g., 0.006% at 900 °C, 0.012% at 950 °C, 0.02% at 1000 °C, 0.035% at 1050 °C, 0.055% at 1100 °C, 0.085% at 1150 °C and 0.127% at 1200 °C respectively, which has been plotted in Fig. 5. It is evident from Fig. 5 that Nb (0.03%) (Table 1) is completely soluble at

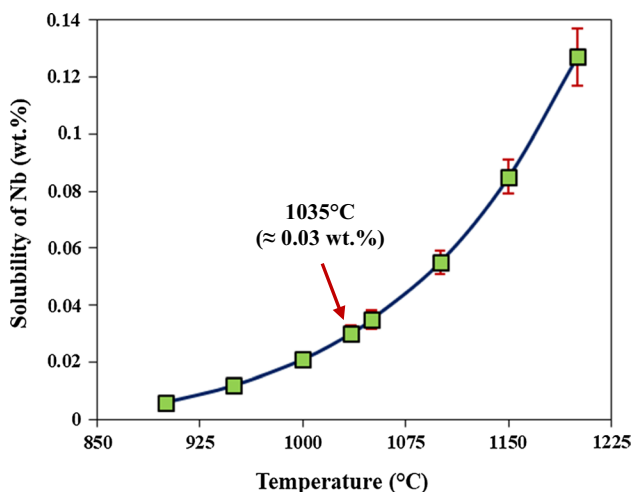


**Fig. 5** Graphical representation of the solubility of Nb in austenite at different temperatures by using Eq. (1)

1035 °C, as denoted by the arrow in Fig. 5. Therefore, it can be said that when the temperature reaches 1000 °C, balance Nb (0.01%) will assist the NbC formation by combining with C as shown in Fig. 4f because Nb is a strong carbide forming element [51–56]. In this connection, it is pertinent to mention here that during soaking at 1200 °C, Nb is complete to be taken into solution depending on the solubility of Nb. It is expected that during air-cooling after hot rolling, supersaturation of solute Nb enhances and precipitation starts at favourable kinetic circumstances. Deformation in the austenite region can also introduce lattice defects like dislocations and vacancies which further assist the diffusional process and also directs the precipitation kinetics. As a consequence, strain-induced precipitation may take place at the prior austenite grain boundaries or defects like dislocations [56].

## 3.2 Mechanical Properties Evaluation

### 3.2.1 Indentation SIZE effect (ISE) on Nanohardness and Elastic Modulus

Table 4 summarises the minimum, maximum and average values of elastic modulus ( $E_m$ ) (GPa) and nanohardness (H) (GPa) for both the hot rolled and air-cooled samples with FRT ≈ 1000 °C and hot-rolled air-cooled followed by isothermally treated samples at 570 °C. After taking almost 20 to 25 indentations at the various spots on the samples the average values were calculated for all the samples. It can be observed from Table 4 that nanohardness values may differ significantly depending upon the pearlite interlamellar spacing and soundness of the surface which is also known as the degree of the perfectness of continuity and parallelism of the lamellae. Therefore, in the pearlite microstructure, an area where the interlamellar spacings are finer is always preferable to a region with coarse pearlite interlamellar spacing. It is noteworthy to mention here that in the case of small interlamellar spacings, the lamellae are expected almost to be perpendicular to the surface of the sample and due to this the microstructure of the surface can be expected to be similar as well as a representative at the indentation depth. It has been reported earlier that the variation in nanohardness values is very similar to the interlamellar spacing values within one pearlite nodule whereas, it may vary significantly for different nodules irrespective of finer interlamellar spacings which are mainly because of variation of the

**Table 4** Minimum, maximum and average values of elastic modulus ( $E_m$ ) and nanohardness (H)

Sample condition	Min. $E_m$ (GPa)	Max. $E_m$ (GPa)	Avg. $E_m$ (GPa)	Min. H (GPa)	Max. H (GPa)	Avg. H (GPa)
HC0-HRAC-FRT 1000 °C	183.39	217.78	204.18 ± 8.66	3.43	5.51	4.45 ± 0.53
HC1-HRAC-FRT 1000 °C	188.46	223.69	204.56 ± 8.66	3.58	5.31	4.48 ± 0.36
HC0-FRT 1000 °C–IH 570 °C	191.03	225.67	206.19 ± 11.34	3.35	5.36	4.49 ± 0.48
HC1-FRT 1000 °C–IH 570 °C	185.65	212.93	199.91 ± 8.61	3.80	5.25	4.39 ± 0.78



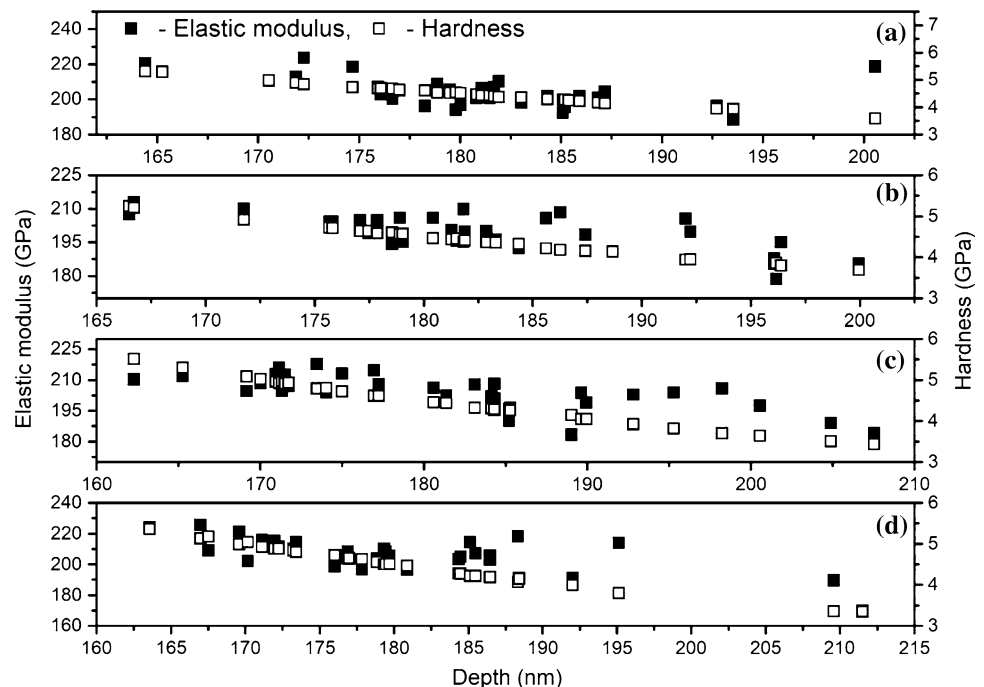
ferrite crystal orientations from one nodule to another and in that case another factor known as cementite lamellae orientation may come into consideration [58]. It has been observed from Table 4 that after isothermal holding, the effective elastic modulus for HC1 steel is less than HC0 steel, which correlates well with the earlier investigations and which may be attributed to the fact that elastic modulus decreases as the thickness of cementite lamellae decreases as evident in Table 3 [59]. It has been reported earlier that the elastic modulus of ferrite is in the range from 260.1 to 306.7 GPa whereas, for cementite it has been observed from 149.3 to 201.0 GPa, depending upon the relevant crystallographic directions [27, 59]. In pure ferrite, the solubility of carbon is extremely low, approximately lower than one carbon atom per thousand iron atoms, but in the case of near eutectoid steel ( $C \approx 0.66$  wt%) with ferrite pearlite microstructure, the solubility of carbon increases significantly due to the presence of cementite ( $\approx 6.67\%$  C) and it may reach up to a value approximately one carbon atom per forty-three iron atoms and there is a chance that a lot of carbon atoms can diffuse to nucleate the pearlite phase, which includes cementite. Therefore, it is expected that the elastic moduli of cementite will be stiffer than ferrite. It is also expected that interstitial carbon atoms in the iron lattice tend to enhance the interatomic spring constants, which further increases the elastic moduli [60]. However, it has been confirmed that interstitial carbon will also contribute to expanding the volume of the lattice, which further results in lowering the elastic moduli [60]. The significant variation in the values of hardness and the similar values of elastic modulus might be attributed to variation in grain sizes, shapes and orientations, whereas these factors have no considerable effect on the elastic modulus [25].

Figure 6 shows typical indentation depth profiles of hardness and elastic modulus of hot rolled air-cooled samples and isothermally treated samples. Each point represents here the average values of hardness and elastic modulus at a particular indentation depth. It is evident that the hot rolled air-cooled samples (Fig. 6a and c) show nearly a linear behaviour whereas, isothermally treated samples (Fig. 6b and d) exhibit a little bilinear behaviour when indentation depth ( $h$ ) is higher than 150 nm which may be attributed with softer substrate effect (SSE) [61]. In this context, it needs to be mentioned that an artificial problem has been already reported while measuring the hardness of high hardness or modulus materials at a small indentation depth [61–63]. It has been observed that the nanohardness values significantly decrease with the increase in indentation depth ( $h$ ) or size for all the samples which may be correlated with ISE. However, the elastic modulus does not follow the same trend as nanohardness values for indentation depth, which agrees well with earlier investigations [61]. It is noteworthy to mention here that the explanation of ISE has been already given by Nix and Gao by developing a model, which is based on the theory of geometrically essential dislocation [61, 64]. Thus, the prediction of the hardness depth profile is possible from Eq. (2) according to Nix Gao model as follows:

$$H = H_0 \sqrt{1 + (h^*/h)} \quad (2)$$

where,  $H_0$  can be defined as the infinite depth hardness or equivalent bulk hardness and  $h^*$  is the characteristic length which depends on the geometry and the material type of

**Fig. 6** Plot showing indentation depth profiles of nanoindentation hardness and elastic modulus of hot rolled and air-cooled samples **a** HC1-HRAC-FRT 1000 °C, **c** HC0-HRAC-FRT 1000 °C and isothermally treated samples **b** HC1-FRT 1000 °C-IH 570 °C, **d** HC0-FRT 1000 °C-IH 570 °C



the indenter tip. Table 5 summarises the values of  $H_0$  from the least-squares fitting of experimentally obtained hardness data by extrapolation method ( $185 < h < 210$  nm) in Eq. (2). Table 5 also includes the values of experimentally obtained Vickers hardness ( $HV_{30}^{Exp.}$ ) and converted Vickers hardness ( $HV_{30}^{Conv.}$ ). A simple correlation was used for the ratio of the area that has been projected (H) to the area of the surface (HV) to convert the experimentally obtained Vickers hardness data with an alteration of the units from  $\text{kgf}/\text{mm}^2$  to GPa, as given by Eq. (3) [61].

$$HV_{30}^{Conv.} = 0.01058 \times HV_{30}^{Exp.} \quad (3)$$

It can be observed from Table 5 that the values of  $HV_{30}^{Conv.}$  and  $H_0$  are quite similar for hot rolled air-cooled samples and isothermally treated samples for both the steels, which agrees well with earlier observations. However, it cannot be overruled that the relationship between  $HV_{30}^{Conv.}$  and  $H_0$  is not well understood yet and is still under consideration [61].

In this context, it is imperative to mention that the experimentally obtained Vickers hardness values ( $HV_{30}^{Exp.}$ ) can be converted to equivalent nanohardness ( $H^{Conv.}$ ) by using another empirical formula proposed by Fischer-Cripps where the unit of the estimated values of  $H^{Conv.}$  will be in MPa [65].

$$H^{Conv.} = HV_{30}^{Exp.} / 0.094495 \quad (4)$$

Table 6 summarises the estimated values of  $H^{Conv.}$  and  $HV_{30}^{Exp.}$  of the two investigated steels obtained from Eq. (4) [65]. It can be seen from Tables 5 and 6 that the estimated values of  $H_0$ ,  $HV_{30}^{Conv.}$  and  $H^{Conv.}$  are in good agreement. This fact further indicates a good correlation of the empirical formulae (Eqs. (2), (3) and (4)) and also confirm the accuracy of the measuring techniques of experimental Vickers hardness and nanohardness values in the present investigation.

Figure 7 reveals the scanning probe microscopic (SPM) image of an indentation on the lamellar structure of pearlite after hot rolling followed by IH at 570 °C. It can be observed from Fig. 7c that, the indentation has been done on the surface with a maximum depth of 126 nm. The higher hardness value signifies the presence of cementite and lower values represent the presence of ferrite in the lamellar configuration of pearlite. It has been observed by researchers that the accuracy in the measured nanohardness values may be

**Table 6** Estimated values of  $H^{Conv.}$  and  $HV_{30}^{Exp.}$  of the two investigated steels from Eq. (4)

Sample condition	$H^{Conv.}$ (GPa)	$HV_{30}^{Exp.}$ (kgf/mm <sup>2</sup> )
HC0-HRAC-FRT 1000 °C	$2.73 \pm 0.56$	$258 \pm 5$
HC1-HRAC-FRT 1000 °C	$2.81 \pm 0.54$	$266 \pm 5$
HC0-FRT 1000 °C–IH 570 °C	$2.49 \pm 0.52$	$235 \pm 4$
HC1-FRT 1000 °C–IH 570 °C	$2.56 \pm 0.72$	$242 \pm 4$

affected depending upon the surface roughness as well as the indentation depth. It has been reported that in the case of ductile materials this affected zone (caused by the surface roughness and indentation size effect) can be reached up to a depth of about a similar size as the finished particle size during the final polishing [58].

### 3.2.2 Analysis in Nanohardness Values: Role of Pearlite Interlamellar Spacing

Figure 8 summarises the values of average nanohardness as well as the standard deviation for the experimental steels after hot rolling air-cooling (HC0-HRAC-FRT 1000 °C & HC1-HRAC-FRT 1000 °C) and hot rolling air-cooling (HRAC) followed by IH treatment (HC0-FRT 1000 °C–IH 570 °C & HC1-FRT 1000 °C–IH 570 °C). It has been observed from Table 4 and Fig. 8 that the minimum nanohardness value is maximum for HC1 steel after hot rolling air-cooling followed by IH at 570 °C (3.80 GPa), whereas the maximum nanohardness value has been noticed in the case of HC0 steel after hot rolling and air-cooling (5.51 GPa). It can be seen from Fig. 8 that the lowest standard deviation in the average nanohardness value has been found in the case of Nb microalloyed steel after HRAC (0.36 GPa) although, the highest standard deviation (0.78 GPa) has been also found in the case of Nb microalloyed steel after hot rolling air-cooling followed by IH (at 570 °C) treatment. Therefore, it can be said that due to this lower interlamellar spacing and finer nodule size throughout the sample, the nanohardness value does not differ much after hot rolling followed by air-cooling (uninterrupted cooling or free cooling). But, after IH at 570°C the ferrite volume percent increases (due to interrupted cooling) and the pearlite volume percentage decreases significantly in HC1 steel (Table 2), which may be since Nb acts as a ferrite stabiliser [44]. As a result of this

**Table 5** Estimated values of  $H_0$ ,  $HV_{30}^{Exp.}$  and  $HV_{30}^{Conv.}$  of the two investigated steels from Eqs. (2) & (3)

Sample condition	$H_0$ (GPa)	$HV_{30}^{Exp.}$ (kgf/mm <sup>2</sup> )	$HV_{30}^{Conv.}$ (GPa)
HC0-HRAC-FRT 1000 °C	$2.68 \pm 0.05$	$258 \pm 5$	$2.72 \pm 0.06$
HC1-HRAC-FRT 1000 °C	$2.75 \pm 0.06$	$266 \pm 5$	$2.81 \pm 0.05$
HC0-FRT 1000 °C–IH 570 °C	$2.35 \pm 0.08$	$235 \pm 4$	$2.49 \pm 0.03$
HC1-FRT 1000 °C–IH 570 °C	$2.41 \pm 0.12$	$242 \pm 4$	$2.56 \pm 0.04$

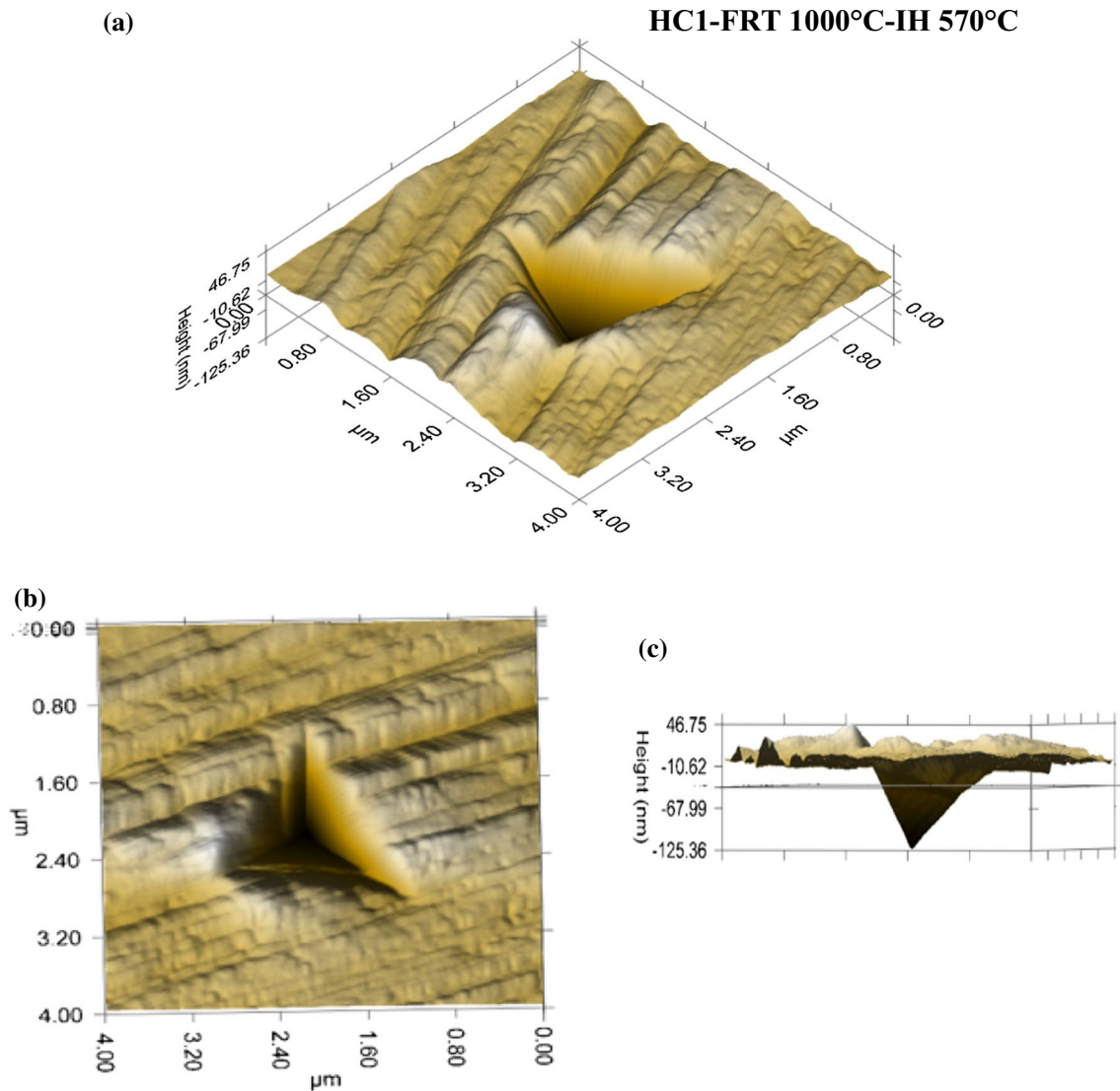


**Fig. 7** SPM 3D images of the morphology of indents of nanohardness measurements

increasing volume percentage of ferrite after IH at 570°C, it is expected that there will be more variation in the ferrite crystal orientations throughout the sample and due to this, the average nanohardness value has been found to fluctuate significantly in case of HC1 steel [58].

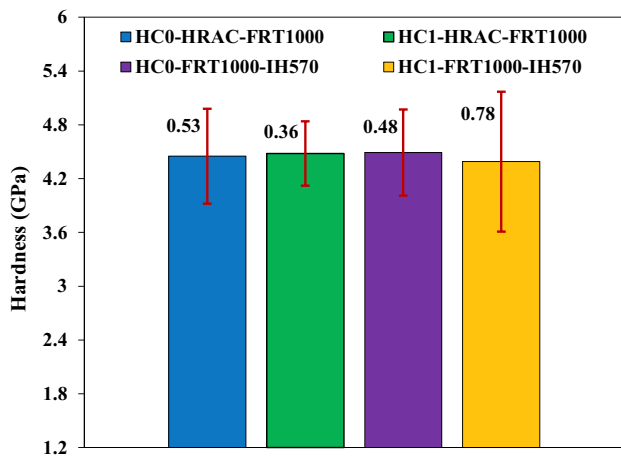
Figure 9 represents the variation of the nanohardness values with pearlite interlamellar spacing at different conditions for both the experimental steels. It can be seen from Fig. 9 that the large variation in the average nanohardness values (standard deviation 0.78 GPa) in the Nb microalloyed steel after IH at 570°C, has been accompanied by the significant variation in the interlamellar spacing (standard deviation 24 nm), which is in well agreement with the earlier investigations [58]. It is also noticeable that the slight variation in interlamellar spacing (standard deviation 10 nm) for Nb microalloyed steel after hot rolling followed by air-cooling

results in the minimum variation in the nanohardness values (standard deviation 0.36 GPa) which is very obvious and is also similar to earlier investigations [58]. Therefore, it can be concluded that these parameters are relevant and can be further utilised to understand the influence of the pearlite interlamellar spacing on the hardness since these average nanohardness values are measured after performing a reasonable set of nanoindentation tests and apparent pearlite interlamellar spacing measurements [58].

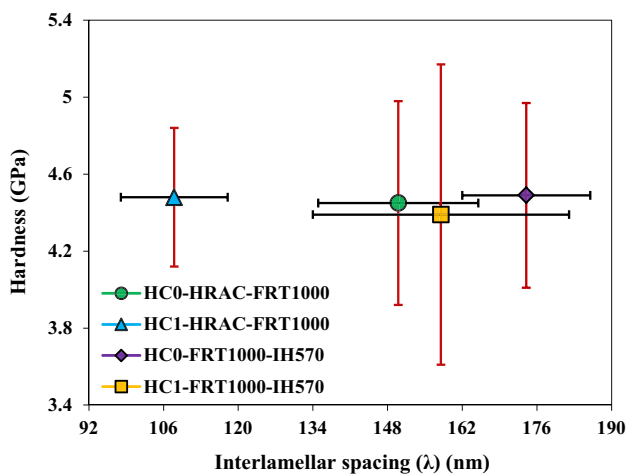
### 3.2.3 Justification of Multiphase from the Microhardness Measurements

Figure 10 represents the SEM micrographs with microhardness values of the low temperature isothermally heat-treated samples. It has been observed that different hardness values



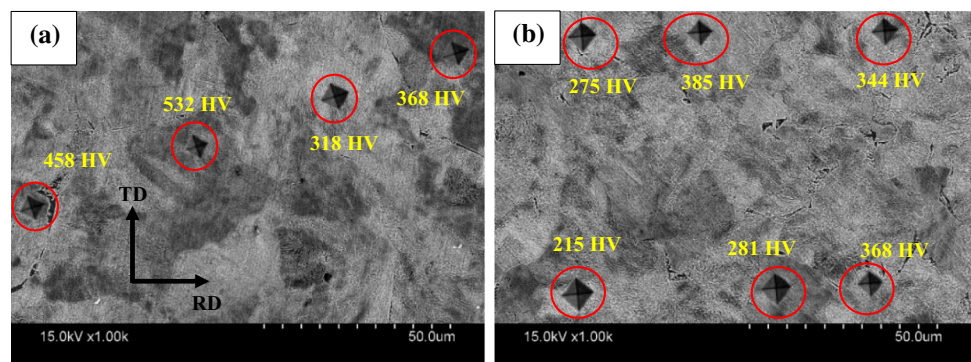


**Fig. 8** The nanohardness values of the experimental steels after hot rolling air-cooling (HC0-HRAC-FRT 1000 °C & HC1-HRAC-FRT 1000 °C) and hot rolling air-cooling followed by isothermal holding treatment (HC0-FRT 1000 °C-IH 570 °C & HC1-FRT 1000 °C-IH 570 °C). The sample variance is exceptionally large (0.36–0.78 GPa)



**Fig. 9** Variation of the nanohardness with the interlamellar spacing of pearlite at different conditions of the experimental steels

**Fig. 10** SEM micrographs with Vickers indentations along with microhardness values of the heat-treated samples **a** HC0-FRT 1000 °C-IH 300 °C and **b** HC1-FRT 1000 °C-IH 300 °C. RD: Rolling direction and TD: Transverse direction



are obtained from different phase constituents corresponding to the different heat-treated samples. It is well known that the indentation size is inversely proportional to the hardness value which means more the harder phase smaller will be the indentation size. The variation in hardness values at different phase (contrast) can be observed in Fig. 10 which depicts the presence of martensite, pearlite, ferrite as well as bainite. It can be noted that the hardness value of 532 HV indicates the evidence of martensite or lower bainite phase [66]. It is evident from Fig. 10 that for HC1 steel the maximum hardness value is < 400 HV whereas, for HC0 steel the maximum hardness value is > 400 HV. This may be attributed to the fact that in HC0 steel, the harder phases like lower bainite or martensite forms in higher volume percentage from the parent austenite phase whereas, in HC1 steel it is expected that the addition of Nb has promoted the ferrite formation (due to free cooling) and thereby marginally reduced the volume percentage of lower bainite or martensite during low temperature IH at 300 °C which is also evident in Figs. 2e and f and 3e and f [32, 44]. The hardness value of around 200 HV to 316 HV in Fig. 10 gives indications of both resolved as well as unresolved pearlite. Thus, it can be mentioned that the hardness values higher than 350 HV are for the bainite/martensite phase whereas, a hardness value less than 200 HV indicates ferrite with some amount of resolved pearlite [66, 67].

### 3.2.4 Engineering Stress–Strain Curves

Figure 11 shows the tensile stress–strain plots for both the hot-rolled air-cooled samples with FRT ≈ 1000 °C and hot-rolled air-cooled followed by heat-treated samples at 570 °C. It is important to note that all curves in Fig. 11 exhibit discontinuous yielding characteristics which is expected in high carbon ferrite-pearlite steels and this behaviour can be explained by a sudden transition in the yielding behaviour with characteristic yield drop followed by a Luders band propagation [68]. Table 7 summarises the values of yield strength ( $\sigma_Y$ ), ultimate tensile strength (UTS), total elongation percentage (TEL) (%),

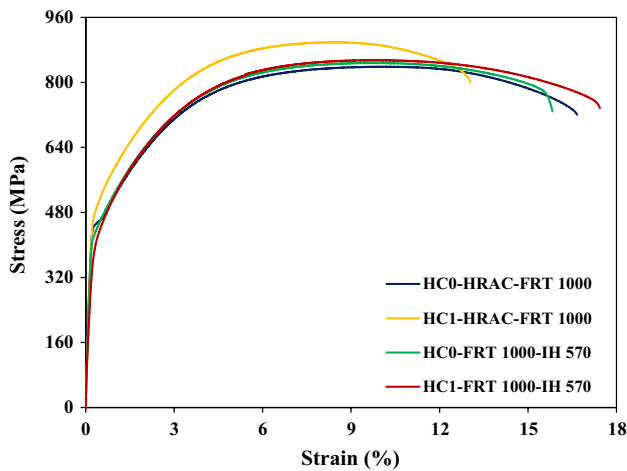


**Fig. 11** Tensile stress–strain curves for various hot rolled air-cooled and isothermally heat-treated samples

yield ratio ( $\sigma_Y/UTS$ ) and product of UTS and TEL ( $MPa \times \%$ ) of the hot-rolled air-cooled samples with  $FRT \approx 1000^\circ C$  and hot-rolled air-cooled followed by isothermally heat-treated samples at  $570^\circ C$  for both the steels. It can be observed that the maximum strength has been obtained for the Nb microalloyed steel after hot rolling followed by air-cooling with  $FRT \approx 1000^\circ C$  which may be attributed to the fact that Nb contributes to the refinement of the interlamellar spacing due to a higher cooling rate than the isothermally treated samples. It can be noticed from Table 3 vis-à-vis Table 7 that a decrease in the interlamellar spacing of 42 nm (from 150 to 108 nm) leads to an enhancement of 49 MPa (from 456 to 505 MPa) in yield strength and 60 MPa (from 839 to 899 MPa) in ultimate tensile strength values for the Nb microalloyed steel after hot rolling followed by air-cooling. It can be observed from Fig. 11 and Table 7 that maximum elongation has been obtained for the Nb microalloyed steel after hot rolling followed by isothermal holding at  $570^\circ C$ . This fact is due to the presence of more amount of ferrite in the final microstructure after hot rolling followed by isothermal holding. In this context, it is noteworthy to mention that isothermal holding near  $P_s$  after hot rolling with  $FRT \approx 1000^\circ C$  leads to the formation of ferrite previously and also since ferrite can be formed during free

cooling before isothermal holding. Nb, being a ferrite stabiliser also stabilise some amount of ferrite in the final microstructure after isothermal holding at  $570^\circ C$ .

### 3.2.5 Validation of the Experimental Results with the Estimated Values

Equation (5) was utilised for the estimation of the ultimate tensile strength (UTS) for all the samples. Whereas, Eqs. (6) and (7) were used to estimate the yield strength at the hardness range from 200 to 300 HV and 300 to 400 HV, respectively [68, 69]. In the same manner, the yield ratio ( $\frac{\sigma_Y}{UTS}$ ) for different samples was calculated using Eq. (8) for different values of hardness. It is well-established that using these equations the highest coefficient of correlation between hardness and strength can be obtained, however, the correlation coefficient did not attain the value of  $R^2 = 0.9$  which indicates a lower interdependence between strength and hardness [69]. It has been already reported that the UTS value obtained from this Eq. (5), can differ (up to  $\pm 125$  MPa) from the strength value obtained from tensile test results [69]. It is noteworthy to mention here that all these equations were used earlier for the estimations of strength from the measured Vickers hardness value where the hardness values were measured under 5 kg load [69]. Although in the present research, the Vickers hardness values were calculated under 30 kg load, it has been found that these equations correlate well with the experimental values obtained from the tensile test results (Table 7 vis-à-vis Table 8).

$$UTS = 2.77HV + 92.754; R^2 = 0.8786 \quad (5)$$

$$\sigma_Y = 1.5703HV + 76.165; R^2 = 0.5694 \quad (6)$$

$$\sigma_Y = 2.5009HV - 181.44; R^2 = 0.7695 \quad (7)$$

$$\frac{\sigma_Y}{UTS} = 0.0006 HV + 0.417; R^2 = 0.2303 \quad (8)$$

**Table 7** Experimental values of yield strength ( $\sigma_Y$ ), ultimate tensile strength (UTS), total elongation (TEL) (%), yield ratio ( $\sigma_Y/UTS$ ) and product of UTS and TEL ( $MPa \times \%$ )

Sample identification	Yield strength ( $\sigma_Y$ ) (MPa)	Ultimate tensile strength (UTS) (MPa)	TEL (%)	Yield ratio ( $\frac{\sigma_Y}{UTS}$ )	Product of UTS and TEL ( $MPa \times \%$ )
HC0-HRAC-FRT $1000^\circ C$	456	839	16	0.54	13,424
HC1-HRAC-FRT $1000^\circ C$	505	899	13	0.56	11,687
HC0-FRT $1000^\circ C$ -IH $570^\circ C$	446	848	16	0.53	13,568
HC1-FRT $1000^\circ C$ -IH $570^\circ C$	437	855	17	0.51	14,535

**Table 8** Values of measured hardness (HV30/20), estimated yield strength ( $\sigma_y$ ), estimated ultimate tensile strength (UTS) and estimated yield ratio ( $\sigma_y$ /UTS)

Sample identification	Measured hardness (HV30/20)	Estimated yield strength ( $\sigma_y$ ) (MPa)	Estimated ultimate tensile strength (UTS) (MPa)	Estimated yield ratio ( $\frac{\sigma_y}{UTS}$ )
HC0-HRAC-FRT 1000 °C	258 ± 5	481 ± 40	807 ± 125	0.57 ± 0.06
HC1-HRAC-FRT 1000 °C	266 ± 5	494 ± 40	830 ± 125	0.58 ± 0.06
HC0-FRT 1000 °C-IH 570 °C	235 ± 4	445 ± 40	744 ± 125	0.56 ± 0.06
HC1-FRT 1000 °C-IH 570 °C	242 ± 4	456 ± 40	763 ± 125	0.56 ± 0.06
HC0-FRT 1000 °C-IH 300 °C	358 ± 10	714 ± 40	1084 ± 125	0.63 ± 0.10
HC1-FRT 1000 °C-IH 300 °C	369 ± 10	741 ± 40	1115 ± 125	0.64 ± 0.10

Table 8 summarises the measured hardness, estimated yield strength, estimated tensile strength and the ratio of estimated yield strength and tensile strength values of different hot rolled as well as hot rolled followed by isothermal holding near  $P_s$  and above  $M_s$  of both high carbon as well as Nb microalloyed steels. It can be seen from Table 8, in all the cases Nb microalloyed steels exhibit higher values of hardness, yield strength and tensile strength. For the hot rolled air-cooled samples (FRT $\approx$ 1000 °C) and isothermally heat-treated samples at 570 °C, this fact may be attributed to the refinement of pearlite interlamellar spacing as well as pearlite colony size and nodule size due to Nb addition, which can be also observed in Figs. 4a and b and also in good agreement with the earlier observations [70, 71]. Whereas, for low-temperature isothermally heat-treated samples, improvement in mechanical properties in Nb bearing steel can be related to the expected formation of niobium carbide or nitride precipitates at 300 °C [54, 72, 73]. Although it has been observed in some high-resolution FESEM micrographs that the occurrence of fine particles, which may be carbides, are less for Nb microalloyed steel than the without Nb microalloyed steel after isothermal holding at 300 °C. It has been reported earlier that NbC precipitates can retard the occurrence of these harmful iron carbide particles which tend to reduce the strength and toughness values of the investigated steels [73]. It has been already reported that the estimated yield ratio obtained by using Eq. (8) shows a minimum dependency about a hardness value of 330 HV. However, it can be observed from Table 7 vis-à-vis Table 8 that, both the experimental and estimated yield ratios correlate well with a maximum deviation of 0.1 and the lower yield ratio ( $\sim$ 0.51 to 0.64) can be associated with the coarse niobium carbide or nitride precipitates in austenite which is also evident in Fig. 4d [51–74]. Therefore, it can be concluded that due to the presence of this first kind of precipitates in the present work, the precipitation strengthening was hindered and as a result work-hardening has been reduced, which further leads to enhancement in estimated tensile strength but with the lower yield ratio [51–75].

### 3.3 Fractography

Figure 12 reveals the FESEM micrographs of the fracture surface of hot rolled air-cooled samples and isothermally treated samples at 570 °C. The fractographic analysis reveals plentiful dimples as well as cup-type of fracture in Fig. 12d which may be related to near-complete spheroidization and thereby indicating purely ductile failure. Nucleation of voids followed by gradual growth and then coalescence of the same result in this cup type fracture which is a typical sign of a specimen showing the ductile fracture [36]. It is noteworthy that the highest amount of total elongation was found in the case of Nb microalloyed samples after hot rolling followed by IH at 570 °C as shown in Table 7, which may be related to the presence of some amount of spheroidized cementite particles as shown in Fig. 3(d). However, the occurrence of flat facets in Fig. 12 is an indication of the presence of fragmented lamellae (also visible in Figs. 3c and d) which were not converted into spheroids [36]. The fracture surface for both the steels after IH near  $P_s$  exhibits a typical river-like pattern which signifies cleavage fracture. Moreover, it can be said that the presence of cleavage facets and non-uniformly distributed shallow dimples on the fractured surface is a clear indication of a mixed type of fracture [75].

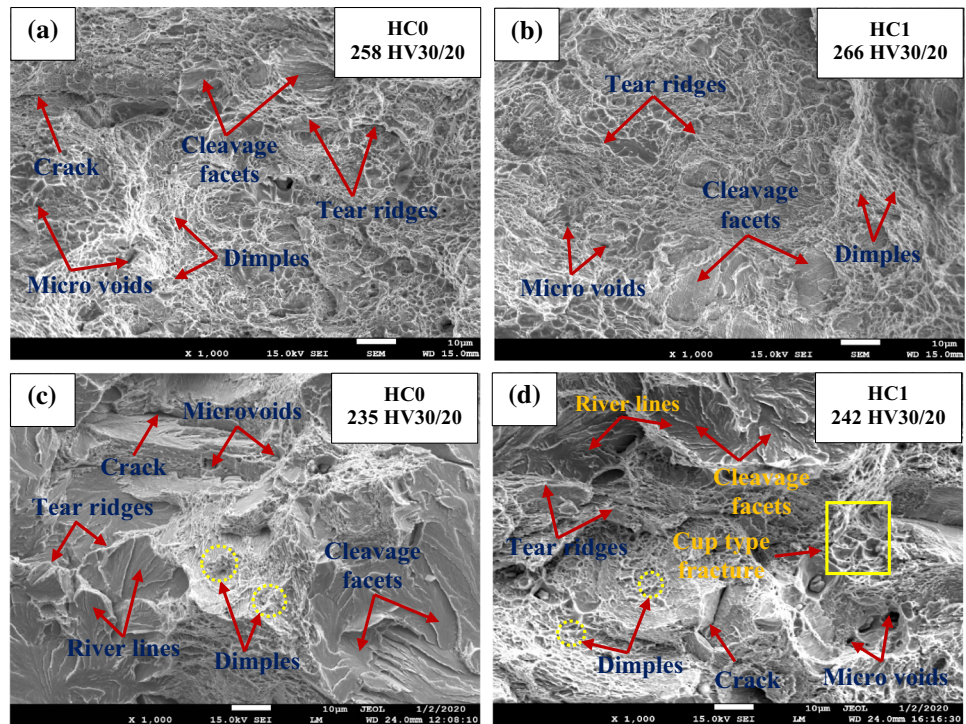
### 4 Conclusions

The most important conclusions derived from this study can be listed below:

1. Hot rolling (FRT $\approx$ 1000 °C) followed by air-cooling as well as isothermal holding at 570 °C leads to a formation of ferrite-pearlite microstructure but with increasing volume percentage of ferrite in both the steels after isothermal holding. Whereas isothermal holding at 300 °C (above  $M_s$ ) results in the formation of bainite predominantly with some amount of martensite (M)/retained austenite (RA), pearlite and ferrite. However, a



**Fig. 12** FESEM micrographs of the fracture surface of hot rolled air-cooled **a** HC0-FRT-1000 °C, **b** HC1-FRT-1000 °C and isothermally treated samples at 570 °C **c** HC0-FRT 1000 °C-IH 570 °C and **d** HC1-FRT 1000 °C-IH 570 °C



significant amount of retained austenite was not detected due to the inadequate amount of Mn and Si.

- The refinement in the values of prior austenite grain size (PAGS), pearlite nodule size (NS), pearlite colony size (PS), pearlite interlamellar spacing ( $\lambda$ ) and cementite thickness (CT) for HC1 steel can be related to the fact that Nb microalloying results in the refinement of all these parameters (PAGS, NS, PS,  $\lambda$  and CT). The refinement in PS, NS,  $\lambda$  and CT for hot-rolled air-cooled samples is related to uninterrupted cooling or free cooling with faster cooling rate whereas, hot rolled air-cooled samples with isothermal heat treatment at 570 °C subjected to interrupted cooling or slower cooling rate. Both fine (~5–25 nm) and coarse NbC precipitates (~30–80 nm) have been observed in HC1 steel in hot rolled and air-cooled condition.
- Nanoindentation test results have shown that maximum average hardness in case of HC1 steel after hot rolling followed by air-cooling which has followed the same trend with those Vickers hardness values. Both the experimental and extrapolation results are almost similar with minor variation and agreed well with earlier observations. The large variation in the average nano-hardness values has been accompanied by a significant variation in the interlamellar spacing. The effective elastic modulus value for HC1 steel after isothermal holding is lower than HC0 steel, which is attributed to the fact that elastic modulus decreases with lowering the thickness of cementite lamellae.
- The microhardness values above 350 HV is an indication of harder phase like bainite whereas, the values lower than 300 HV confirms softer pearlite and the values less than 250 HV indicate the other softer phases like ferrite and resolved pearlite. Although the microhardness value of more than 500 HV indicates the harder phase like martensite. The size of the microindentations decreases with the presence of harder phases and vice versa.
- The values of yield strength and ultimate tensile strength are higher in the case of hot rolled air-cooled samples than those of isothermally heat-treated samples at 570 °C, which is due to the refinement in interlamellar spacing. However, the ductility is increased after isothermal holding due to the presence of more volume percentage of ferrite than pearlite. The experimental tensile test results correlate well with the estimated values.

## References

- G. Mandal, C. Roy, S.K. Ghosh, S. Chatterjee, *J. Alloy. Compd.* **705**, 817 (2017)
- N. Amirjani, M. Ketabchi, M. Eskandari, M. Hizombor, *Met. Mater. Int.* (2020). <https://doi.org/10.1007/s12540-020-00841-3>
- M. Opiela, *Arch. Mater. Sci. Eng.* **28**, 377 (2007)
- H. Zhao, J. Qi, G. Liu, R. Su, Z. Sun, *J. Mater. Res. Technol.* **9**, 11319 (2020)
- H.J. McQueen, N.D. Ryan, *Mater. Sci. Eng. A* **322**, 43 (2002)
- G.E. Dieter, D.J. Bacon, *Mechanical Metallurgy*, 1st edn. (McGraw-Hill, New York, 1986), pp. 488–508

7. H. Beladi, P.D. Hodgson, *Scripta Mater.* **56**, 1059 (2007)
8. P.J. Wray, *Metall. Mater. Trans. A* **13**, 125 (1982)
9. S. Serajzadeh, A.K. Taheri, *Mater. Design* **23**, 271 (2002)
10. S.J. Lee, Y.K. Lee, *Mater. Design* **29**, 1840 (2008)
11. E. Anelli, *ISIJ Int.* **32**, 440 (1992)
12. A.K. Giumelli, M. Militzer, E.B. Hawbolt, *ISIJ Int.* **39**, 271 (1999)
13. J.S. Park, Y.K. Lee, *Scripta Mater.* **57**, 109 (2007)
14. J.G. Speer, J.R. Michael, S.S. Hansen, *Metall. Trans. A* **18**, 211 (1987)
15. T. Sakuma, R.W.K. Honeycombe, *Met. Sci.* **18**, 449 (1984)
16. S. Behera, R.K. Barik, M.B. Sk, R. Mitra, D. Chakrabarti, *Mater. Sci. Eng. A* **764**, 138256 (2019)
17. D.A. Porter, K.E. Easterling, G.D.W. Smith, *Acta Metall.* **26**, 1405 (1978)
18. E.M. Taleff, J.J. Lewandowski, B. Pourladian, *J. Mater. Sci.* **54**, 25 (2002)
19. X. Zhang, A. Godfrey, X. Huang, N. Hansen, Q. Liu, *Acta Mater.* **59**, 3422 (2011)
20. M. Jung, W. Cho, J. Park, J.G. Jung, Y.K. Lee, *Mater. Charact.* **94**, 161 (2014)
21. H. Rastegari, A. Kermanpur, A. Najafifzadeh, *Mater. Design* **67**, 217 (2015)
22. T.W. Hong, S.I. Lee, J.H. Shim, M.G. Lee, J. Lee, B. Hwang, *Met. Mater. Int.* **27**, 3935 (2021)
23. C. Tonteling, K.J. Palmer, F.B. Helfer, R. Todd, J.J. Blum, *Process for producing patented steel wire*, US Patent 5595617 (1998)
24. A.S. Ghorabaei, S.S.G. Banadkouki, *Mater. Sci. Eng. A* **700**, 562 (2017)
25. T.H. Pham, J.J. Kim, S.E. Kim, *J. Constr. Steel Res.* **99**, 121 (2014)
26. Y. Choi, W.Y. Choo, D. Kwon, *Scripta Mater.* **45**, 1401 (2001)
27. H. Ghaffarian, A.K. Taheri, S. Ryu, K. Kang, *Curr. Appl. Phys.* **16**, 1015 (2016)
28. R. Rodriguez, I. Gutierrez, *Mater. Sci. Eng. A* **361**, 377 (2003)
29. L. Qian, M. Li, Z. Zhou, H. Yang, X. Shi, *Surf. Coat. Tech.* **195**, 264 (2005)
30. T.A. Zubkova, I.L. Yakovleva, L.E. Karkina, I.A. Veretennikova, *Met. Sci. Heat. Treat.* **56**, 330 (2014)
31. D. Ye, Z. Wang, *Int. J. Fatigue* **23**, 85 (2001)
32. A. Mkaddem, R. Bahloul, P.D. Santo, A. Potiron, *J. Mater. Process. Tech.* **180**, 1 (2006)
33. T.N. Baker, *Ironmak. Steelmak.* **43**, 264 (2016)
34. G.F. Vander Voort, *Pract. Metallogr.* **52**, 419 (2015)
35. T. Sakai, A. Belyakov, R. Kaibyshev, H. Miura, J.J. Jonas, *Prog. Mater. Sci.* **60**, 130 (2014)
36. C. Prasad, P. Bhuyan, C. Kaithwas, R. Saha, S. Mandal, *Mater. Design* **139**, 324 (2018)
37. D.V. Edmonds, K. He, F.C. Rizzo, B.C.D. Cooman, D.K. Matlock, J.G. Speer, *Mater. Sci. Eng. A* **438–440**, 25 (2006)
38. S.G. Liu, S.S. Dong, F. Yang, L. Li, B. Hu, F.H. Xiao, Q. Chen, H.S. Liu, *Mater. Design* **56**, 37 (2014)
39. A.N. Lopez, J. Hidalgo, J. Sietsma, M.J. Santofimia, *Mater. Design* **188**, 108484 (2020)
40. E.P.D. Silva, D.D. Knijf, W. Xu, C. Fojer, Y. Houbaert, J. Sietsma, R. Petrov, *Mater. Sci. Tech.* **31**, 808 (2015)
41. S. Samanta, P. Biswas, S. Giri, S.B. Singh, S. Kundu, *Acta Mater.* **105**, 390 (2016)
42. A.N. Lopez, J. Hidalgo, J. Sietsma, M.J. Santofimia, *Mater. Charact.* **128**, 248 (2017)
43. Z. Yang, H. Wang, Y. Ji, in *Proceedings of the HSLA Steels 2015, Microalloying 2015 & Offshore Engineering Steels 2015*, ed. by The Chinese Society for Metals (CSM) and Chinese Academy of Engineering (CAE). Hangzhou, 11–13 November 2015 (Springer, Cham, 2016), p. 987
44. T. Nebel, D. Eifler, *Sadhana* **28**, 187 (2003)
45. S.M.C.V. Bohemen, M.J. Santofimia, J. Sietsma, *Scripta Mater.* **58**, 488 (2008)
46. J.A.D.C. Junior, D.B. Santos, *J. Mater. Res. Technol.* **2**, 93 (2013)
47. A.J. Clarke, J.G. Speer, M.K. Miller, R.E. Hackenberg, D.V. Edmonds, D.K. Matlock, F.C. Rizzo, K.D. Clarke, E.D. Moor, *Acta Mater.* **56**, 16 (2008)
48. G. Gao, H. Zhang, X. Gui, P. Luo, Z. Tan, B. Bai, *Acta Mater.* **76**, 425 (2014)
49. B. Jiang, X. Hu, L. Zhou, H. Wang, Y. Liu, F. Gou, *Met. Mater. Int.* **27**, 319 (2021)
50. K. Hausmann, D. Krizan, K.S. Hahn, A. Pichler, E. Werner, *Mater. Sci. Eng. A* **588**, 142 (2013)
51. S. Shanmugam, N.K. Ramiseti, R.D.K. Misra, T. Mannering, D. Panda, S. Jansto, *Mater. Sci. Eng. A* **460–461**, 335 (2007)
52. S. Shanmugam, R.D.K. Misra, T. Mannering, D. Panda, S.G. Jansto, *Mater. Sci. Eng. A* **437**, 436 (2006)
53. X.D. Wang, W.Z. Xu, Z.H. Guo, L. Wang, Y.H. Rong, *Mater. Sci. Eng. A* **527**, 3373 (2010)
54. A. Guo, R.D.K. Misra, J. Xu, B. Guo, S.G. Jansto, *Mater. Sci. Eng. A* **527**, 3886 (2010)
55. L. Fan, T. Wang, Z. Fu, S. Zhang, Q. Wang, *Mater. Sci. Eng. A* **607**, 559 (2014)
56. Z. Jia, R.D.K. Misra, R.O. Malley, S.J. Jansto, *Mater. Sci. Eng. A* **528**, 7077 (2011)
57. K. Balasubramanian, A. Korupa, J.S. Kirkaldy, *Metall. Trans. A* **23**, 729 (1992)
58. J. Debehets, J. Tacq, A. Favache, P. Jacques, J.W. Seo, B. Verlinden, M. Seefeldt, *Mater. Sci. Eng. A* **616**, 99 (2014)
59. M. Guziewski, S.P. Coleman, C.R. Weinberger, *Acta Mater.* **144**, 656 (2018)
60. S.A. Kim, W.L. Johnson, *Mater. Sci. Eng. A* **452–453**, 633 (2007)
61. Y. Takayama, R. Kasada, Y. Sakamoto, K. Yabuuchi, A. Kimura, M. Ando, D. Hamaguchi, H. Tanigawa, *J. Nucl. Mater.* **442**, S23 (2013)
62. G.M. Pharr, J.H. Strader, W.C. Oliver, *J. Mater. Res.* **24**, 653 (2009)
63. G.M. Pharr, E.G. Herbert, Y. Gao, *Annu. Rev. Mater. Res.* **40**, 271 (2010)
64. W.D. Nix, H. Gao, *J. Mech. Phys. Solids* **46**, 411 (1998)
65. A.C. Fischer-Cripps, *Nanoindentation*, 3rd edn. (Springer Inc., New York, 2011), pp. 26–27
66. A. Ebrahimi, S.S.G. Banadkouki, *J. Alloy. Compd.* **708**, 43 (2017)
67. E. Fereiduni, S.S.G. Banadkouki, *J. Alloy. Compd.* **577**, 351 (2013)
68. Y. Wang, Y. Tomota, T. Ohmura, W. Gong, S. Harjo, M. Tanaka, *Acta Mater.* **196**, 565 (2020)
69. M. Gasko, G. Rosenberg, *Mat. Eng.* **18**, 155 (2011)
70. H.J. Kestenbach, G.S. Martins, *Metall. Trans. A* **15**, 1496 (1984)
71. P.C. Liu, Z.X. Wang, J.H. Cong, R.D.K. Misra, X.M. Wang, A.M. Guo, Y.Q. Zhang, *Mater. Lett.* **279**, 128520 (2020)
72. G.M. Sim, J.C. Ahn, S.C. Hong, K.J. Lee, K.S. Lee, *Mater. Sci. Eng. A* **396**, 159 (2005)
73. H. Wu, B. Ju, D. Tang, R. Hu, A. Guo, Q. Kang, D. Wang, *Mater. Sci. Eng. A* **622**, 61 (2015)
74. S.S. Nayak, R.D.K. Misra, J. Hartmann, F. Siciliano, J.M. Gray, *Mater. Sci. Eng. A* **494**, 456 (2008)
75. S. Ghosh, S. Mula, *Mater. Sci. Eng. A* **646**, 218 (2015)

**Publisher's Note** Springer Nature remains neutral with regard to jurisdictional claims in published maps and institutional affiliations.